ISSN 2580-0817

Effect of Argon Gas Flow Rate on Crystal Structure, Morphology, and Optical Properties of CIGS Film for Photodetector Applications

Nurul Lathi'i Fatul Chamidah[1], Fadilah Wulan Cahyani[1], I Gusti Ayu Isnaini Fatha Ramadhani[1], Erma Surya Yuliana[1], Nasikhudin[1], Safwan Abd. Aziz[2], Nandang Mufti[1,3]*

[1]*Department of Physics, Faculty of Mathematics and Natural Sciences, Universitas Negeri Malang, Malang 65145, Indonesia*

[2]*Laser Center, Ibnu Sina Institute for Scientific and Industrial Research, Universiti Teknologi Malaysia, 81310 Skudai, Johor Bahru, Malaysia*

[3]*Center of Advanced Material for Renewable Energy, Universitas Negeri Malang, Malang, 65145, Indonesia*
**Corresponding author:nandang.mufti.fmipa@um.ac.id*

Article history:
Received: 30 July 2025 / Received in revised form: 23 September 2025 / Accepted: 29 September 2025
Available online 19 October 2025

ABSTRACT

CIGS material can be used as a material for photodetector applications. The deposition of CIGS thin films remains challenging. Generally, argon is used as a gas to bombard the CIGS material through the sputtering method. This study fabricated photodetectors by varying the argon gas flow rate (50-80 sccm) to investigate its effect on device performance. XRD, SEM, UV-Vis, and photoresponse tests were characterized. Structural analysis using XRD showed a weak (112) diffraction peak, indicating that the resulting film was not fully crystalline, but rather consisted of a nanocrystalline phase, even partly amorphous, with small crystallite sizes. According to the SEM analysis, the thin film thickness increased from 1.005 μm to 1.283 μm with increasing argon gas flow rate. The UV-VIS characterization analysis exhibited a maximum absorbance at a wavelength of 234 nm and a band gap decreasing from 2.43 to 2.30 eV. The photoresponse analysis revealed that thicker absorber layers responded more slowly to light exposure, indicating a reduction in charge carrier mobility. The current and voltage response times were found to range from 3.01 to 5.01 seconds and 2.18 to 4.35 seconds, respectively. Therefore, it can be stated that argon gas flow rate significantly plays a role in the performance of CIGS thin film-based photodetectors.

Keywords: *Argon gas, CIGS, flow rate, photodetector, sputtering.*

I. Introduction

Photodetectors are one of the key components in modern multifunctional technology [1] which can convert optical signals into electrical signals [2], [3]. Devices used to detect light, typically in the form of photons, convert light signals into electrical signals that electronic circuits can then measure. Photodetectors are widely used in a diverse range of applications, including optical communication systems, imaging devices (such as digital cameras), solar cells, and scientific instruments, each tailored to different applications and performance requirements. The different types of photodetectors include photodiodes, photoconductors, phototransistors, and photovoltaic cells. For photovoltaic-type photodetectors, the structure of the device is very similar to that of a solar cell configuration [4]. Therefore, the performance of the photodetector can be optimized by utilizing semiconductor materials that have a high absorption coefficient and charge carrier [5]. Semiconductor materials with a high absorption coefficient are often utilized in solar cells, such as CIGS (Copper Indium Gallium Selenide).

DOI: 10.17977/um016v9i2p464

Currently, CIGS has been explored beyond its conventional application in solar cells. This p-type semiconductor has attracted considerable attention due to its promising properties. As a p-type material used in photovoltaic applications, $Cu(In,Ga)Se_2$ (CIGS) shows great potential as a light-absorbing layer owing to its high absorption coefficient [6] and adjustable band gap energy spanning 1.04 eV - 3.5 eV [7]. The band gap in CIGS makes it easy to excite electrons because the energy required is the least. The advantages of CIGS material, besides its high absorption coefficient, are that it exhibits a good surface recombination speed and favorable radiation properties [8].

CIGS thin film can be deposited through several methods. Some of the techniques used in CIGS thin film deposition are non-vacuum methods, such as sol-gel [9], spin coating [10], spray coating, selenating, and electrodeposition [11]. Furthermore, vacuum deposition methods can be broadly divided into two primary categories: chemical vapor deposition (CVD) [12] and physical vapor deposition (PVD) [13], [14]. Research on CIGS conducted by Duchlatet *et al.* [15] Using electrodeposition and selenation methods is time-consuming and less efficient. Therefore, in this study, the deposition of CIGS involved sputtering. Method Sputtering is a method included in the PVD in thin film deposition (thin film) on a substrate, so it is widely used because it allows reasonable control of the composition of the film by adjusting the target sputtering [16], [17]. The growth of thin films requires relatively low temperatures and minimizing material loss during deposition. The parameters involved in the sputtering process include time, power, temperature, pressure, gas type, and gas flow rate. Argon gas is commonly utilized due to its large atomic mass, odorless and colorless characteristics, chemical inertness, and relatively low cost [12]. During the sputtering process, argon is ionized into plasma composed of electrons, positively charged ions, and neutral molecules under partial pressure within the plasma chamber. The more positively charged electrons and ions hit the target, the more target atoms are sputtered towards the substrate, forming a thin film. So, the more argon gas that flows, the thicker the layer will be.

Research on CIGS by Rahmawati *et al.* with the electrodeposition method produced an efficiency of 0.04% [18]. Minimal results will be more efficient if applied as a photodetector. Research conducted by Goddess *et al*., who examined the deposed CIGS layer using the spin coating, generated a voltage based on photoresponse testing, which is about 0.012 mV [10]. In addition, CIGS/CdS-based photoresponse research using a non-vacuum method conducted by Mandate *et al.* produces a current value of about 0.5 mA/cm^2 [19]. Based on several previous studies, the generated current remains relatively low, determined by operating conditions including power, pressure, time, temperature, gas type, and gas flow rate. A similar observation was reported by Serrar *et al.* [20], who investigated the effect of argon gas flow rate on TiO_2 materials. However, despite several previous studies, there are still few that examine the impact of argon gas flow rate on the thickness of the CIGS layer as a photodetector in sputtering. Therefore, this study investigated the influence of argon gas flow rate on the sputtering process, focusing on the thickness of the CIGS layer, morphology, crystal structure, optical properties, and photoresponse of CIGS films. The composition of the CIGS film fabrication used in this study is the FTO/CIGS/ITO substrate layer. The deposition of the CIGS layer uses RF sputtering, while the ITO layer is carried out using DC sputtering by varying the flow rate of argon gas during the deposition of the CIGS layer, which aims to determine the effect of the flow rate of argon gas on the crystal structure, morphology, and optical properties of the CIGS layer. In addition, this study aims to study the effect of argon gas flow rate on the thickness of CIGS layers for photodetector applications.

II. Material and Methods

The research methodology outlines the chronological framework of the study, including the research design, experimental procedures (presented as algorithms, pseudocode, or other formats), instruments, and analytical techniques employed to address the research problem. The experimental methods should be described in sufficient detail to enable replication by other researchers. Whenever applicable, the sources of reagents and materials used in the study should also be specified.

Firstly, the FTO substrate is washed twice using an ultrasonic cleaner. Initially, the FTO substrate is cleaned with soapy water. It is then washed using acetone and rinsed using DI Water. After the FTO substrate is washed, it is then dried using tissue. Second, the deposition of the layer starts with the CIGS layer, and then the ITO is layered on it. All thin-film depositions were performed using the sputtering technique, with the corresponding sputtering parameters displayed in Table 1.

Table 1. Parameters of the sputtering deposition process

Parameters	CIGS (RF)	ITO (DC)
Pressure (Pa)	1	1
Power (W)	100	60
Time (minutes)	240	45
Temperature (°C)	200	100
Flow rate argon gas (sccm)	50, 60, 70, and 80	70

The deposition of the CIGS layer is carried out by varying the flow rate of argon gas, namely 50, 60, 70, and 80 sccm (standard cubic centimeters per minute). In this study, several variables are used, including free, controlled, and bound variables. The independent variable was the argon gas flow rate used during CIGS layer deposition, while the controlled variables included pressure, power, deposition time, and temperature. The bound variables include crystal structure, morphology, CIGS layer thickness, optical properties, and the sample's response to light.

1. Fabrication

The CIGS fabrication process is carried out by deposition of 2 layers, namely the CIGS and ITO layers. The FTO layer acts as a conductive substrate, then the CIGS layer as an absorber layer, while the ITO layer acts as a contact. An illustration of the fabrication of the CIGS sample is shown in Figure 1.

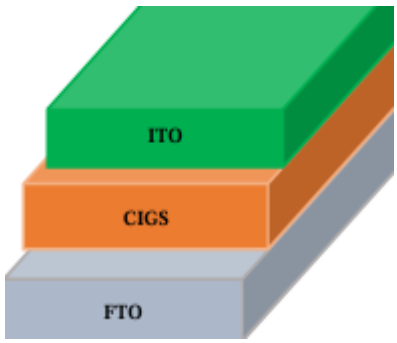

Fig. 1. FTO/CIGS/ITO coating

All thin-film depositions were carried out using the sputtering technique. The deposition of the CIGS layer was performed by RF sputtering, whereas the ITO layer was deposited using DC sputtering under different parameter settings. The deposition parameters are presented in Table 1. During the deposition of the CIGS layer, variations in the argon gas flow rate were investigated at 50, 60, 70, and 80 sccm.

2. Characterization

Characterization was performed on CIGS samples prepared under different argon gas flow rates. X-ray diffraction (XRD) was used to determine the crystal structure, while scanning electron microscopy (SEM) was employed to examine the surface morphology and thin-film porosity. Cross-sectional SEM analysis was conducted to measure the deposited film thickness, and energy-dispersive X-ray spectroscopy (EDX) was used to identify the elemental composition of the film surface. Additionally, ultraviolet-visible (UV-Vis) spectroscopy was carried out to evaluate the band gap energy and optical absorbance. Additionally, a photodetector was tested using a solar simulator to determine the sample's response to the presence of light.

3. Analytical Techniques

The test results in this study were analyzed using several software programs. The OriginPro 2018 software is used to generate the graph from the results of XRD characterization, as well as the photoresponse graph of current density and voltage. Subsequently, to analyze the thickness and surface morphology of the thin films, the ImageJ software was used. To find the porosity value, use Origin software. Eq. (1) is used to calculate the porosity value.

$$\text{Porosity} = \frac{\text{Pore volume}}{\text{Total volume}} \times 100\% \quad \text{.....} \quad (1)$$

Band gap energy was determined using the Tauc plot equation (Equation (2))

$$(\alpha h\nu)^2 = A(h\nu - E_g) \quad \text{.....} \quad (2)$$

The value of α represents the material's absorption coefficient, h is Planck's constant, v denotes the photon frequency, E corresponds to the photon energy, and E_g represents the band gap energy [21], [22].

III. Results and Discussions

1. Structural Characterization (XRD)

XRD characterization was performed on four CIGS samples with varying argon gas flow rates, namely 50, 60, 70, and 80 sccm. The results of the XRD characterization are presented in Figure 2. In the samples deposited at lower argon flow rates (50 and 60 sccm), weak diffraction peaks corresponding to the (112) plane at 27.3 were detected, indicating the presence of very fine nanocrystals. X-ray diffraction (XRD) analysis only shows a weak diffraction peak on the (112) plane corresponding to the CIGS chalcopyrite phase. The absence of other peaks such as (220)/(204) or (312)/(116) indicates that the film has a low degree of crystallinity, with the degree of crystallinity estimated at around 20–30%. The average crystallite size calculated using the Scherrer equation for the (112) peak is in the range of 20–25 nm. Meanwhile, at higher flow rates (70 and 80 sccm), no sharp peaks were observed, and the broad hump in the range of 2θ = 25-30° suggests that the film is predominantly amorphous. This behavior arises because higher argon pressure reduces ion bombardment energy, limiting surface diffusion of sputtered atoms and preventing ordered

lattice formation. Consequently, films become increasingly amorphous at high flow rates. Therefore, the crystallinity of the CIGS films can be classified as nanocrystalline at lower argon flow rates and more amorphous at higher flow rates. This trend is consistent with previous studies that reported a decrease in crystallinity with increasing argon flow due to reduced ion bombardment energy [23] and contrasts with Chamidah *et al*., who showed that higher substrate temperatures improve CIGS crystallinity by enhancing atomic diffusion. Thus, deposition parameters that lower atomic energy (e.g., high gas flow) promote amorphous structures, while those that increase energy (e.g., high temperature) favor crystalline growth [24].

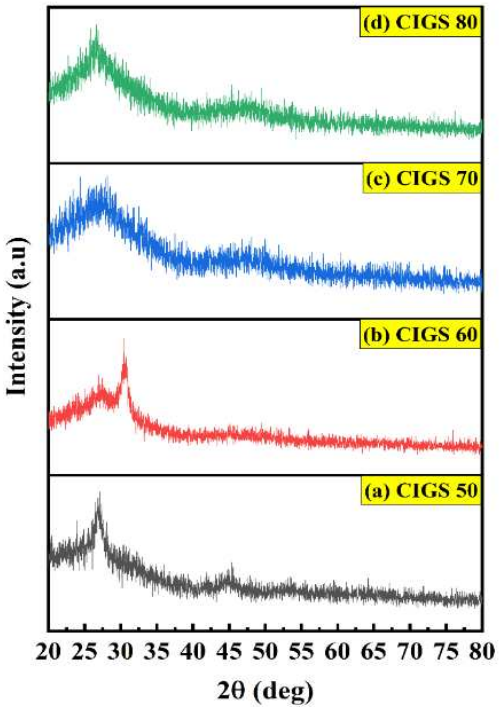

Fig. 2. CIGS layer XRD yield: a) 50, b) 60, c) 70, and d) 80 sccm

2. *Morphology of the CIGS Layer*

The morphology of the CIGS layer was characterized using SEM. Figure 3 displays the surface morphology and cross-sectional view of the CIGS layer with a magnification of 100,000 times at the variation in the flow rate of argon gas, namely a) 50, b) 60, c) 70, and d) 80 sccm. Based on the figure of the three layers of the CIGS, it can be concluded that the layers deposited by the Sputtering have an even and uniform result. In comparison to deposition carried out using the electrodeposition method, which results in a rough sample surface and non-uniform grains [15].

In addition, the thickness of the CIGS layer can be determined by SEM testing cross-section. CIGS layer thickness by varying the flow rate of argon gas at the moment of Sputtering, known by conducting testing cross-section. Based on Figure (a) 50 sccm, (b) 60 sccm, (c) 70 sccm, (d) 80 sccm, the thickness of the CIGS layer with variations in flow rate of argon gas is 1.005 µm, 1.078 µm, 1.195 µm, 1.283 µm (Table 2). The results of these measurements tend to be thinner when compared to previous studies. The flow rate of argon gas has a significant influence on film thickness and surface morphology [20]. The thickness of the CIGS absorber layer, according to the research conducted by Khoshsirat *et al*., is in the range of 1-4 µm [25]. CIGS coatings should ideally have a thickness range of 1-4 µm to be able to respond well to

light. The SEM characterization results were also used to determine the porosity level based on surface morphology observations. Figure 4 presents a three-dimensional graph illustrating the porosity distribution of CIGS thin films under different conditions.

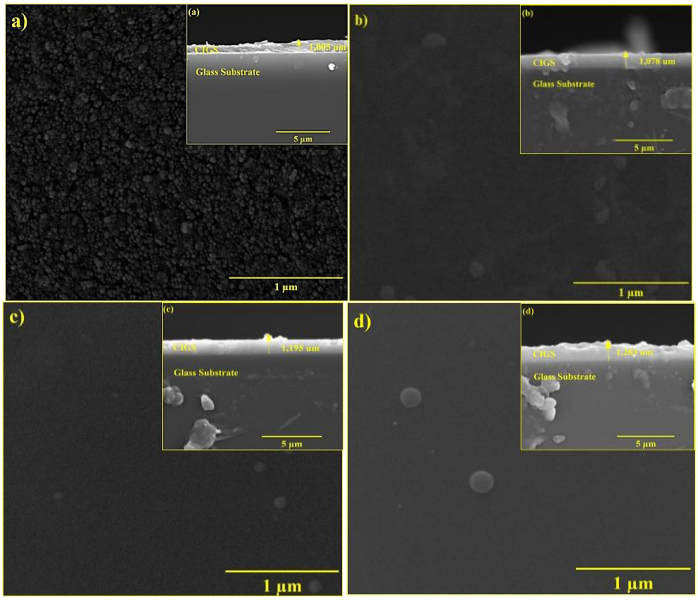

Fig. 3. SEM results accompanied by yield insets cross-section on CIGS layers: (a) 50, (b) 60, (c) 70, and (d) 80 sccm

Table 2. Variation of flow rate to CIGS layer thickness

Name sample	Thickness (µm)
CIGS 50	1.005
CIGS 60	1.078
CIGS 70	1.195
CIGS 80	1.283

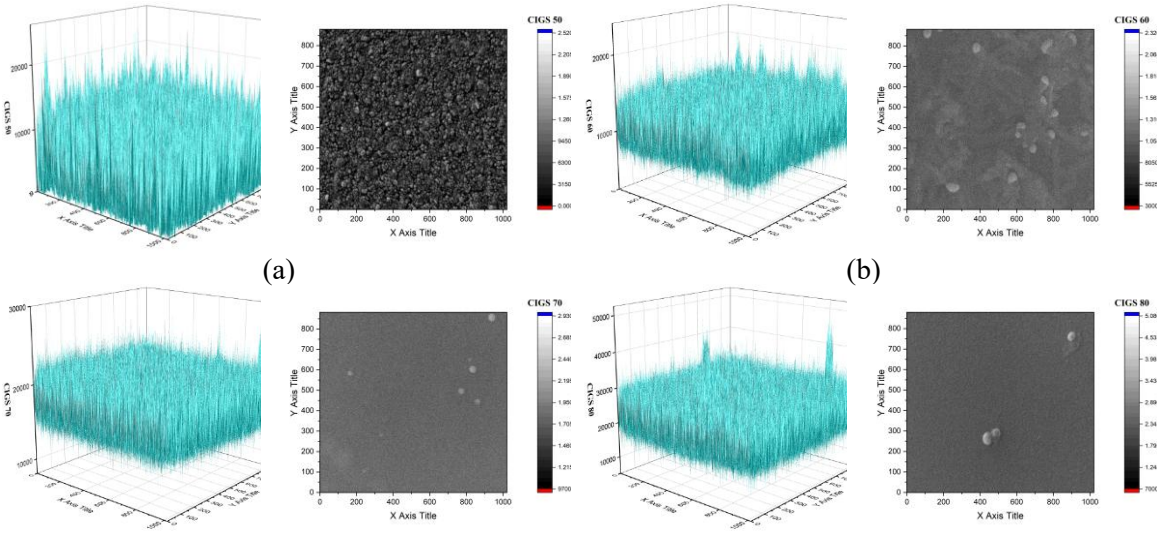

Fig. 4. Porosity distribution of CIGS layers: (a) 50, (b) 60, (c) 70, and (d) 80 sccm

To calculate the porosity value of the CIGS layer, Eq. (1) is used. Table 3 shows the CIGS thin-film porosity calculation results for various variations.

Table 3. SEM analysis of CIGS thin film porosity

Name sample	Porosity (%)
CIGS 50	77.33
CIGS 60	60.22
CIGS 70	58.97
CIGS 80	56.45

Based on the morphological analysis presented in Table 3, the CIGS 50 thin film exhibited the highest porosity of 77.33%. A higher porosity value indicates a larger active surface area [26]. The SEM characterization results shown in Figure 4 confirm that the CIGS thin film with the highest porosity has the potential to increase charge recombination. In addition, surface morphology provides information about the elemental composition of the material, as presented in Table 3. EDX analysis was conducted to identify the types and contents of elements on the surface of the thin film [27] and to ensure its purity from possible contaminants.

EDX analysis confirmed the presence of all CIGS elements with a non-uniform atomic distribution. The highest atomic intensity is obtained in the element Selenium (Se). This is because the band gap depends on the ratio of [Ga]/([Ga] + [In]) (GGI) [28]. Based on the results of EDX characterization, the content ratio of Ga/(In+Ga) was obtained for each sample, as shown in Table 4. It can be seen that the GGI content ratio is very small compared to the results obtained by Wu *et al.* when the ratio of Ga/(In+Ga) is about 0.3, and the Band gap approx. 1.14 eV [29]. When the ratio of Ga/(In + Ga) is below 0.3, the shift of the conductive band will be close to the Fermi energy, so that the electrons will not move to the n-type semiconductor but join the hole, thus increasing the probability of recombination [30]. Whereas, when the ratio of Ga/(In + Ga) increases, the conduction band shifts away from Fermi's energy, thus reducing the likelihood of recombination [31], [32]. The GGI ratio of less than 0.3 has an effect on light absorbance. In the CIGS system, the band gap varies with different Ga/(In+Ga) ratios [33]. EDX analysis verified the presence of Cu, In, Ga, and Se, with Ga/(In+Ga) ratios ranging from 0.10 to 0.17. This compositional variation is directly related to the band gap widening observed in the optical analysis.

Table 4. Elemental composition with EDX characterization of the CIGS layer

Name sample	Cu (%)	In (%)	Ga (%)	Se (%)	Ga/(In+Ga) (%)
CIGS 50	25.9	18.1	3.9	52.1	0.17
CIGS 60	22.5	17.1	3.1	57.3	0.15
CIGS 70	19.1	20.7	3.3	56.8	0.13
CIGS 80	15.0	25.3	3.0	56.7	0.10

3. CIGS Absorbance and Band Gap.

The optical properties, including the absorbance value and band gap, of a material are measured using Ultraviolet-Visible (UV-Vis) spectroscopy. Uv-Vis characterization involves the

interaction of light with the material by varying the flow rate of argon gas. The absorbance values of each sample are shown in Figure 5.

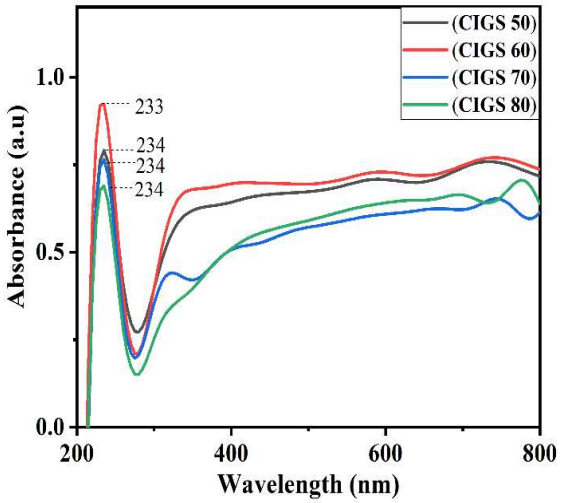

Fig. 5. CIGS Layer absorbance graph with variations of the flow rate of argon gas

In the testing process, there is an interaction between the material and light with a specific wavelength (usually in the range of 200 nm to 900 nm), so that the UV-Vis spectroscopy instrument can measure the light absorbed, transmitted, or reflected by the sample at each wavelength [34]. Figure 5 shows the absorbance of the CIGS layer with variations in the flow rate of argon gas in the wavelength range of 200-800 nm. CIGS samples deposed using a flow rate of argon gas 50 SCCM have a peak of 233 nm, 60 SCCM is at a peak of 234 nm, 70 SCCM is at a peak of 234 nm, and 80 SCCM is at a peak of 234 nm. The flow rate of argon gas has a considerable effect on the optical properties of the thin film [20]. This wavelength range is consistent with the findings reported by Julie *et al*., which states that the CIGS layer has a wave absorption of about 200-1050 nm [35]. In the 400-600 nm wavelength range, the absorbance process of the CIGS sample is still ongoing and begins to decline in the 700 nm range. This is in accordance with research conducted by Harith *et al*., which states that the absorption is still constant in the wavelength range of 400 to 600 nm [36].

In addition to calculating the absorbance values, the UV-Vis characterization results were also used to determine the band gap energy using a Tauc plot ahv^2 versus hv. The Tauc plot method is employed to determine the band gap energy of semiconductor materials through absorbance data analysis and can be applied to both crystalline and amorphous nanomaterials [37]. Figure 6 and Table 5 show the Tauc plot graph ahv^2 Vs hv on the CIGS sample with variations flow rate of argon gas. Based on Table 5, if the absorbance increases, there is a decrease in the band gap value. The value of the band gap is important because light can be absorbed by the sample if it has an energy greater than the value of the band gap [38]. From the results of this study, the Band gap CIGS for all variations are in the range of 2.30 eV to 2.43 eV. This is in accordance with research by Roy *et al.,* which states that in the chalcopyrite alloy system Cu(In, Ga, Al)$(Se,S)_2$, Ribbon gaps vary from 1.04 eV to about 3.5 eV [39].

The optical absorption spectrum obtained from UV-Vis measurements show a shift in the absorption edge with increasing Ga content. The band gap values estimated using Tauc plots are in the range of 2.30 to 2.43 eV. This value is higher than the theoretical prediction (1.09–1.12 eV for GGI 0.10–0.17) regarding to nanocrystalline/amorphous nature of the films, which introduces localized defects and causes band tailing, which broadens the absorption edge and shifts the

apparent optical gap. Furthermore, this indicates that microstructural disorder and defects strongly influence the optical response.

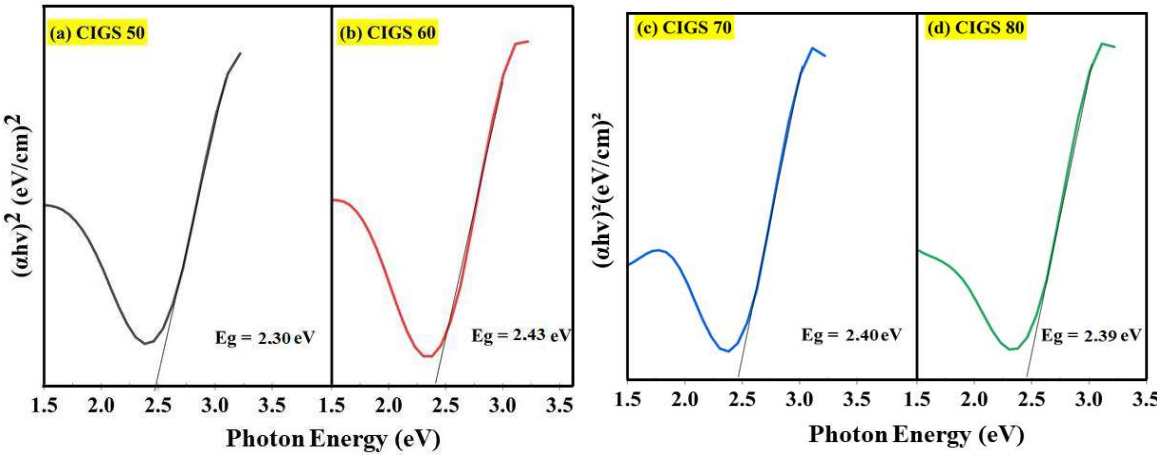

Fig. 6. Result fitting band gap (a) 50, (b) 60, (c) 70, and (d) 80 sccm

Table 5. Variations in flow rate of argon gas with maximum absorbance and value of band gap

Name sample	Maximum absorbance (nm)	Band gap (eV) value
CIGS 50	233	2.30
CIGS 60	234	2.43
CIGS 70	234	2.40
CIGS 80	234	2.39

4. CIGS Photodetector

CIGS-based photodetector testing refers to the ability of a sample to detect and respond to light. This test is conducted to determine how quickly the sample responds to light exposure. Photodetector testing is carried out by alternately exposing the sample to light for 10 seconds and keeping it in darkness for another 10 seconds. This cycle is repeated with a solar simulator with an intensity of 100 mW/cm² to determine the sample's response time. Figure 7 shows a graph of current photoresponse results with variations in the flow rate of argon gas, namely 50, 60, 70, and 80 sccm, respectively.

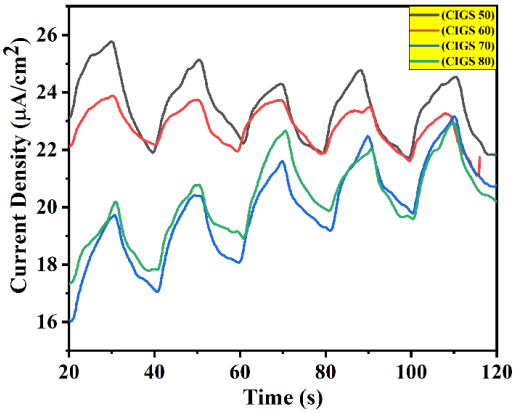

Fig. 7. Photoresponse graph of current and time relationship (I-t) of various variations flow rate

Figure 8 shows the photoresponse graph of the current relationship to time (I-t). It is known that all samples show a good response when exposed to light on. This is characterized by an ascending graph, while when it is not illuminated (light off) it is characterized by a descending graph. The response time of the entire sample when the light on and off is shown in Table 6. The greater the flow rate of argon gas, the slower the light response time (time rise).

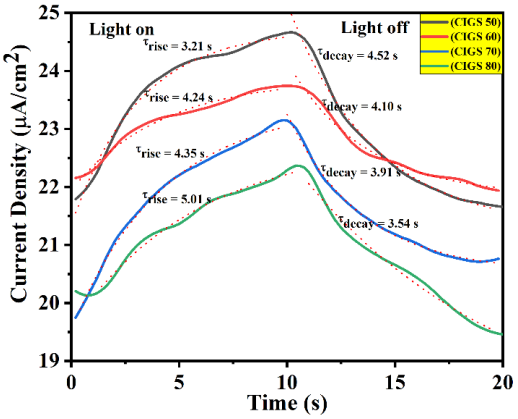

Fig. 8. Current to time relationship sample response chart

Table 6 summarizes the transient response times obtained from the V–t and I–t curves, which show consistent results. The rise time ranges from 2.18 to 5.01 s, while the decay time ranges from 2.59 to 4.52 s. A linear increase in the rise time when exposed to light is observed, and a linear decrease in the decline time when the light is turned off. According to Table 7, the rise time (light on) is consistently faster than the decline time (light off). This asymmetry can be explained by the existence of trap states within the film. Under light-off conditions, electrons remain trapped in a stable local state, resulting in slower recombination and longer decline times. Conversely, under light-on conditions, trapped electrons can be readily excited along with newly formed charge carriers, resulting in faster current and voltage increases. Similar behavior was also reported by Akshana *et al*., who showed that the optical response is highly dependent on the morphology, trap density, and metal composition of the material [25].

Table 6. CIGS layer current response time

Name sample	Light On (second)	Light Off (second)
CIGS 50	3.01	4.52
CIGS 60	4.24	4.10
CIGS 70	4.35	3.91
CIGS 80	5.01	3.54

Table 7. CIGS layer voltage response time

Name sample	Light On (second)	Light Off (second)
CIGS 50	2.18	4.31
CIGS 60	2.83	3.47
CIGS 70	3.62	2.87
CIGS 80	4.35	2.59

Figure 8 shows the photocurrent response of devices. In comparison with previous reports, ZnO-based photodetectors exhibited photocurrent values of 5.7μA/cm^2 [40]. In this work, the CIGS-based thin films demonstrated a significantly higher photocurrent of around 25.8 μA/cm^2. Similarly, Figure 9 and Figure 10 displays the photovoltage response, where devices show 0.35 mV, substantially higher than the 0.012 mV reported for CIGS films deposited by spin coating [10]. These results indicated that the sputtered CIGS films studied here provide superior photoresponse characteristics in terms of both current and voltage.

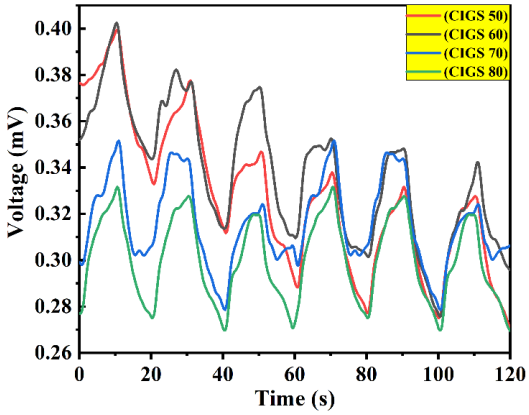

Fig. 9. Photoresponse graph of the voltage-to-time relationship (V-t) of various flow rate variations

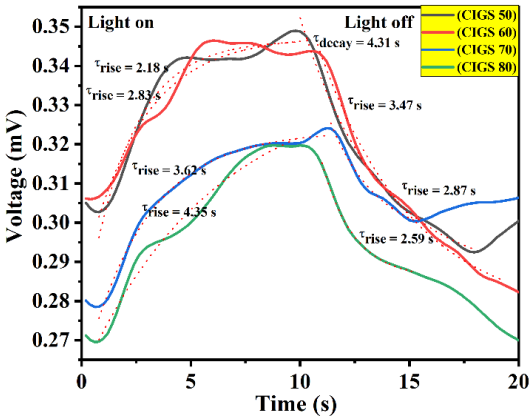

Fig. 10. Voltage-to-time relationship response graph

Although the developed device exhibits higher photocurrent and photovoltaic values compared to previous reports, the response time (2–5 s) is still slower than many state-of-the-art photodetectors. This behavior is in contrast to the findings of Fuad *et al*., who reported a faster response (0.98 s) in CIGS photodetectors when deposition time was optimized [42]. In comparison, ZnO nanorod/CuSCN-based ultraviolet photodetectors respond in the order of milliseconds [43], Perovskite-based photodetectors are capable of achieving response times below 100 ms [44], and even solution-processed ZnO nanocrystal-based devices can achieve sub-microsecond responses [45]. The slower response in the device is because carrier transport is dominated by trap states. Structural analysis also confirmed the presence of nanocrystalline to amorphous phases with high porosity, which introduce carrier traps and prolong the transient response time.

These findings suggest a trade-off between sensitivity and speed. Films with high porosity or disorder can enhance steady-state photocurrent through increased light scattering

and effective surface area, but result in slower temporal response. To overcome this limitation, further optimizations such as post-deposition annealing (in a Se atmosphere or vacuum), surface passivation, adjusting the absorber layer thickness, and heterojunction engineering are required. These efforts are expected to reduce trap density, increase crystallinity, and accelerate the optical response of CIGS films.

IV. Conclusions

CIGS thin films deposited by the RF sputtering method at various argon flow rates exhibited nanocrystalline to semicrystalline structures with some amorphous phases, as confirmed by XRD, which only showed a weak (112) peak with an average crystallite size of ~20–25 nm. SEM analysis showed a porous surface morphology with a thickness increasing from 1.005 μm at 50 sccm to 1.283 μm at 80 sccm, while EDX results confirmed the presence of Cu, In, Ga, and Se elements with a Ga/(In+Ga) ratio of 0.10–0.17. The UV-Vis spectrum showed a band gap widening from 2.30 to 2.43 eV with increasing Ga content, higher than theoretical predictions due to the presence of nanocrystalline and amorphous phases. Photoresponse tests showed a photocurrent of about 25.8 μA/cm² and a photovoltaic of 0.35 mV, higher than some previous reports, although the response time (2–5 s) is relatively slow due to trap states and porosity. This study was limited to the characterization of the structure, morphology, optics, and photoresponse without a more detailed analysis of electrical transport or device integration, and only used the RF sputtering method with a narrow variation of argon flow rate. Therefore, further research is needed to explore different deposition conditions, interface engineering, and more comprehensive electrical measurements to optimize the performance of CIGS-based photodetectors.

Acknowledgment

This research was supported by DRTPM Kemendikbudristek 2024 under Grant No. 11.6.102/UN32.14.1/LT/2024. The authors gratefully acknowledge the financial support that made this work possible.

References

[1] C. Yang, G. Wang, M. Liu, F. Yao, and H. Li, "Mechanism, material, design, and implementation principle of two-dimensional material photodetectors," *Nanomaterials*, vol. 11, no. 10, p. 2688, Oct. 2021, doi: 10.3390/nano11102688.

[2] Z. Bielecki, K. Achtenberg, M. Kopytko, J. Mikołajczyk, J. Wojtas, and A. Rogalski, "Review of photodetectors characterization methods," *Bulletin of the Polish Academy of Sciences Technical Sciences*, pp. 140534–140534, Feb. 2022, doi: 10.24425/bpasts.2022.140534.

[3] S.C. Ray, "Application and uses of graphene," in *Applications of Graphene and Graphene-Oxide Based Nanomaterials*, Elsevier, 2015, pp. 1–38. doi: 10.1016/B978-0-323-37521-4.00001-7.

[4] Y. Zhao, C. Li, and L. Shen, "Recent advances on organic-inorganic hybrid perovskite photodetectors with fast response," *InfoMat*, vol. 1, no. 2, pp. 164–182, Jun. 2019, doi: 10.1002/inf2.12010.

[5] D. Banerjee and K.K. Chattopadhyay, "Hybrid inorganic organic perovskites," in *Perovskite Photovoltaics*, Elsevier, 2018, pp. 123–162. doi: 10.1016/B978-0-12-812915-9.00005-8.

[6] S. Siebentritt, L. Gütay, D. Regesch, Y. Aida, and V. Deprédurand, "Why do we make Cu(In,Ga)Se2 solar cells non-stoichiometric?," *Solar Energy Materials and Solar Cells*, vol. 119, pp. 18–25, Dec. 2013, doi: 10.1016/j.solmat.2013.04.014.
[7] J. Ramanujam and U.P. Singh, "Copper indium gallium selenide based solar cells – a review," *Energy Environ. Sci.*, vol. 10, no. 6, pp. 1306–1319, 2017, doi: 10.1039/C7EE00826K.
[8] R. Daroowalla, R.R. Rangaraju, L. Lin, and N.M. Ravindra, "Temperature dependence of energy gap in semiconductors—influence on solar cell performance," in *TMS 2021 150th Annual Meeting & Exhibition Supplemental Proceedings*, The Minerals, Metals & Materials Society, Ed., in The Minerals, Metals & Materials Series. , Cham: Springer International Publishing, 2021, pp. 259–268. doi: 10.1007/978-3-030-65261-6_23.
[9] H.M. Mirabad, A. Nemati, M.A. Faghihi-Sani, M.F. Hasanabadi, and H. Abdoli, "Effect of YSZ sol-gel coating on interaction of Crofer22 APU with sealing glass for solid oxide fuel/electrolysis cell," *Journal of Alloys and Compounds*, vol. 847, p. 156496, Dec. 2020, doi: 10.1016/j.jallcom.2020.156496.
[10] A.S.P. Dewi, N. Mufti, Arramel, B.H. Arrosyid, Sunaryono, and Aripriharta, "Synthesis and characterization of CIGS/ZnO film by spin coating method for solar cell application," *AIP Conference Proceedings*, vol. 2231, no. April, 2020, doi: 10.1063/5.0002493.
[11] E.S. Yuliana, M.A. Wahyudi, R. Kurniawan, Nasikhudin, and N. Mufti, "Effect of electrodeposition time on microstructure, morphology, and optical properties of CIGS films," *risal. fis.*, vol. 5, no. 1, pp. 40–46, Jan. 2025, doi: 10.35895/rf.v5i1.22.
[12] G.T. West and P.J. Kelly, "Influence of inert gas species on the growth of silver and molybdenum films via a magnetron discharge," *Surface and Coatings Technology*, vol. 206, no. 7, pp. 1648–1652, Dec. 2011, doi: 10.1016/j.surfcoat.2011.08.025.
[13] A.A. Solovyev, N.S. Sochugov, S.V. Rabotkin, A. V. Shipilova, I.V. Ionov, A.N. Kovalchuk, and A.O. Borduleva, "Application of PVD methods to solid oxide fuel cells," *Applied Surface Science*, vol. 310, pp. 272–277, Aug. 2014, doi: 10.1016/j.apsusc.2014.03.163.
[14] Z. Zakaria, Z.A. Mat, S.H. Abu Hassan, and Y. Boon Kar, "A review of solid oxide fuel cell component fabrication methods toward lowering temperature," *Int J Energy Res*, vol. 44, no. 2, pp. 594–611, Feb. 2020, doi: 10.1002/er.4907.
[15] A. Duchatelet, E. Letty, S. Jaime-Ferrer, P.P. Grand, F. Mollica, and N. Naghavi, "The impact of reducing the thickness of electrodeposited stacked Cu/In/Ga layers on the performance of CIGS solar cells," *Solar Energy Materials and Solar Cells*, vol. 162, no. December 2016, pp. 114–119, 2017, doi: 10.1016/j.solmat.2016.12.045.
[16] J. Xu, H. Cai, G. Hao, L. Zhang, Z. Song, W. Long, and L. Wang, "Characterization of high–valence Mo–doped PrBaCo2O5+ cathodes for IT–SOFCs," *Journal of Alloys and Compounds*, vol. 842, p. 155600, Nov. 2020, doi: 10.1016/j.jallcom.2020.155600.
[17] J. N. Wen, R.J. Wu, Y.H. Mi, N. Zhang, Z.H. Lin, Y.Q. Li, and S.F. Yang, "Effect of Ti as co-sputtering target on microstructure and mechanical properties of FeCoNi(CuAl)0.2 high-entropy alloy thin films," *Materials Chemistry and Physics*, vol. 296, p. 127214, Feb. 2023, doi: 10.1016/j.matchemphys.2022.127214.
[18] H. Rahmawati, M.T.H. Abadi, S. Zulaikah, and N. Mufti, "Electrodeposition technique to fabrication CIGS using pure selenium and SeO2 as selenium source," *Mal. J. Fund. Appl. Sci.*, vol. 18, no. 3, pp. 367–373, Aug. 2022, doi: 10.11113/mjfas.v18n3.2489.

[19] S. Mandati, B.V. Sarada, S.R. Dey, and S.V. Joshi, "Enhanced photoresponse of Cu(In,Ga)Se2/CdS heterojunction fabricated using economical non-vacuum methods," *Electron. Mater. Lett.*, vol. 11, no. 4, pp. 618–624, Jul. 2015, doi: 10.1007/s13391-014-4387-9.

[20] H. Serrar, F.Z. Mecibah, I. Kribes, Y. Bouachiba, A. Mammeri, A. Bouabellou, and R. Aouati, "Argon flow rate effects on the optical waveguide properties of DC sputtered TiO2 thin films," *Optical Materials*, vol. 135, no. November 2022, p. 113259, 2023, doi: 10.1016/j.optmat.2022.113259.

[21] A. Ashery, A.A. M. Farag, A.E.H. Gaballah, G. Said, and W.A. Arafa, "Nanostructural, optical and heterojunction characteristics of PEDOT^{TM}/ZnO nanocomposite thin films," *Journal of Alloys and Compounds*, vol. 723, pp. 276–287, 2017, doi: 10.1016/j.jallcom.2017.06.260.

[22] B. Xiao, "Synthesis and application of ZnO/conductive polymer poly (3,4-ethylenedioxythiophene) (ZnO-PEDOT) nanocomposite for photodegrdation of methyl orange," *International Journal of Electrochemical Science*, vol. 17, 2022, doi: 10.20964/2022.05.38.

[23] M. Ahmadipour, M. Arjmand, M.F. Ain, Z.A. Ahmad, and S.Y. Pung, "Effect of Ar:N2 flow rate on morphology, optical and electrical properties of CCTO thin films deposited by RF magnetron sputtering," *Ceramics International*, vol. 45, no. 12, pp. 15077–15081, 2019, doi: 10.1016/j.ceramint.2019.04.245.

[24] N.L.F. Chamidah, N. Mufti, A.S. Dewi, A.A. Permanasari, and Sunaryono, "Effect of temperature to fabrication cigs solar cell using the sputtering method," *E3S Web Conf.*, vol. 473, p. 01004, 2024, doi: 10.1051/e3sconf/202447301004.

[25] N. Khoshsirat, N.A. Md Yunus, M.N. Hamidon, S. Shafie, and N. Amin, "Analysis of absorber layer properties effect on CIGS solar cell performance using SCAPS," *Optik*, vol. 126, no. 7–8, pp. 681–686, 2015, doi: 10.1016/j.ijleo.2015.02.037.

[26] A. Noor, M. Hamdini, S. Ramadina, and Y. Tiandho, "Dye-sensitized solar cell-based photovoltaic thermal for ethanol distillation: A narrative review," *Jurnal Geliga Sains: Jurnal Pendidikan Fisika*, vol. 8, no. 2, p. 123, Jan. 2021, doi: 10.31258/jgs.8.2.123-131.

[27] V.D. Hodoroaba, *Energy-dispersive X-ray spectroscopy (EDS)*, no. X. Elsevier Inc., 2019. doi: 10.1016/B978-0-12-814182-3.00021-3.

[28] U. Künecke, M. Schuster, and P. Wellmann, "Analysis of compositional gradients in cu(In,ga)(s,se)2 solar cell absorbers using energy dispersive x-ray analysis with different acceleration energies," *Materials*, vol. 14, no. 11, 2021, doi: 10.3390/ma14112861.

[29] C.H. Wu, P.W. Wu, J.H. Chen, J.Y. Kao, and C.Y. Hsu, "Effect of selenization processes on CIGS solar cell performance," *Journal of Nanoscience and Nanotechnology*, vol. 18, no. 7, pp. 5074–5081, 2017, doi: 10.1166/jnn.2018.15279.

[30] N. Mufti, A.S.P. Dewi, R.K. Putri, A. Taufiq, H. Nur, "Selenization process in simple spray-coated CIGS film," *Ceramics International*, vol. 48, no. 15, pp. 21194–21200, 2022, doi: 10.1016/j.ceramint.2022.04.015.

[31] A.C. Badgujar, R.O. Dusane, and S.R. Dhage, "Cu(In,Ga)Se2 thin film solar cells produced by atmospheric selenization of spray casted nanocrystalline layers," *Solar Energy*, vol. 209, no. August, pp. 1–10, 2020, doi: 10.1016/j.solener.2020.08.080.

[32] K. Fotis, "Modelling and simulation of a dual-junction CIGS solar cell using Silvaco Atlas," *Technical Report*, no. December, p. 123, 2012.

[33] X. Lv, Z. Zheng, M. Zhao, H. Wang, and D. Zhuang, "Investigation on preparation and performance of high Ga CIGS absorbers and their solar cells," *Materials*, vol. 16, no. 7, pp. 1–10, 2023, doi: 10.3390/ma16072806.
[34] M.S.H. Akash and K. Rehman, "Thermogravimetric analysis". *In Essentials of pharmaceutical analysis. Springer, Singapore. Chapter 19; 215-221*. 2019.
[35] J. Goffard, C. Colin, F. Mollica, A. Cattoni, C. Sauvan, P. Lalanne, and S. Collin, "Light trapping in ultrathin CIGS solar cells with nanostructured back mirrors," *IEEE Journal of Photovoltaics*, vol. 7, no. 5, pp. 1433–1441, 2017, doi: 10.1109/JPHOTOV.2017.2726566.
[36] H. Jaafer, A. Kadhum, and A. Al-Samarei, "Effect of annealing temperature on UV-visible spectra of CIGS films prepared by drop coating method," *Chem. Eng. Chem. Res*, vol. 2, no. 12, pp. 924–931, 2015.
[37] P.R. Jubu, O.S. Obaseki, A. Nathan-Abutu, F.K. Yam, Y. Yusof, and M.B. Ochang, "Dispensability of the conventional Tauc's plot for accurate bandgap determination from UV–vis optical diffuse reflectance data," *Results in Optics*, vol. 9, no. July, p. 100273, 2022, doi: 10.1016/j.rio.2022.100273.
[38] I. Benigno, "Pengaruh optimasi celah pita energi dan ketebalan lapisan tipe–i pada efisiensi sel surya silikon amorf sambungan P-i-n," *Repository Institut Teknologi Sepuluh Nopember*, p. 78, 2017.
[39] P. Roy, A. Ghosh, F. Barclay, A. Khare, and E. Cuce, "Perovskite solar cells: A review of the recent advances," *Coatings*, vol. 12, no. 8, pp. 1–24, 2022, doi: 10.3390/coatings12081089.
[40] J. Lu, C. Xu, J. Dai, J. Li, Y. Wang, Y. Lin, and P. Li, "Improved UV photoresponse of ZnO nanorod arrays by resonant coupling with surface plasmons of Al nanoparticles," *Nanoscale*, vol. 7, no. 8, pp. 3396–3403, 2015, doi: 10.1039/C4NR07114J.
[41] A.P. Sreekala, A. Nadukkandy, S. Shaji, D. A. Avellaneda, J. A. Aguilar-Martínez, and B. Krishnan, "AgSbS2-xSex thin films: Structure, composition, morphology and photodetection properties," *Materials Today Communications*, vol. 27, no. March, 2021, doi: 10.1016/j.mtcomm.2021.102362.
[42] M.Y. Fuad, A.A. Salim, N.L.I.F. Chamidah, A.S.P. Dewi, E.S. Yuliana, Nasikhudin, and N. Mufti, "Optimizing CIGS-based photodetectors: Influence of deposition time on structural, optical, and light response characteristics," *J. Electron. Mater.*, Sep. 2025, doi: 10.1007/s11664-025-12308-5.
[43] S.M. Hatch, J. Briscoe, and S. Dunn, "A self-powered ZnO-Nanorod/CuSCN UV photodetector exhibiting rapid response," *Advanced Materials*, vol. 25, no. 6, pp. 867–871, Feb. 2013, doi: 10.1002/adma.201204488.
[44] F. Mei, D. Sun, S. Mei, J. Feng, Y. Zhou, J. Xu, and X. Xiao, "Recent progress in perovskite-based photodetectors: the design of materials and structures," *Advances in Physics: X*, vol. 4, no. 1, p. 1592709, Jan. 2019, doi: 10.1080/23746149.2019.1592709.
[45] T. Zhang, J. Yu, Y. Deng, N. Tian, and P. Gao, "Fast response ultraviolet photodetectors based on solution-processed ZnO nanocrystals," *Sci. China Technol. Sci.*, vol. 58, no. 8, pp. 1328–1332, Aug. 2015, doi: 10.1007/s11431-015-5870-8.